CORA Cork Open Research Archive
Cartlann Taighde Oscailte Chorcaí

Title	Supercapattery based on binder-free Co3 (PO4)2·8H2O multilayer nano/microflakes on nickel foam
Authors	Shao, Han;Padmanathan, Narayanasamy;McNulty, David;O'Dwyer, Colm;Razeeb, Kafil M.
Publication date	2016-09-30
Original Citation	Shao, H., Padmanathan, N., McNulty, D., O'Dwyer, C. and Razeeb, K. M. (2016) 'Supercapattery based on binder-free Co3 (PO4) 2· 8H2O multilayer nano/microflakes on nickel foam', ACS Applied Materials and Interfaces, 8(42), pp. 28592-28598. doi:10.1021/acsami.6b08354
Type of publication	Article (peer-reviewed)
Link to publisher's version	10.1021/acsami.6b08354
Rights	© 2016, American Chemical Society. This document is the unedited Author's version of a Submitted Work that was subsequently accepted for publication in ACS Applied Materials and Interfaces, copyright © American Chemical Society, after peer review. To access the final edited and published work see http://pubs.acs.org/doi/abs/10.1021/acsami.6b08354
Download date	2026-10-31 04:32:49
Item downloaded from	https://hdl.handle.net/10468/3191

UCC
University College Cork, Ireland
Coláiste na hOllscoile Corcaigh

ACS APPLIED MATERIALS & INTERFACES

Subscriber access provided by UNIV COLL CORK

Article

Supercapattery based on binder-free Co3(PO4)2·8H2O multilayer nano/ microflakes on nickel foam

Han Shao, Narayanasamy Padmanathan, David McNulty, Colm O'Dwyer, and Kafil M. Razeeb

ACS Appl. Mater. Interfaces, **Just Accepted Manuscript** • DOI: 10.1021/acsami.6b08354 • Publication Date (Web): 30 Sep 2016

Downloaded from http://pubs.acs.org on October 5, 2016

Just Accepted

"Just Accepted" manuscripts have been peer-reviewed and accepted for publication. They are posted online prior to technical editing, formatting for publication and author proofing. The American Chemical Society provides "Just Accepted" as a free service to the research community to expedite the dissemination of scientific material as soon as possible after acceptance. "Just Accepted" manuscripts appear in full in PDF format accompanied by an HTML abstract. "Just Accepted" manuscripts have been fully peer reviewed, but should not be considered the official version of record. They are accessible to all readers and citable by the Digital Object Identifier (DOI®). "Just Accepted" is an optional service offered to authors. Therefore, the "Just Accepted" Web site may not include all articles that will be published in the journal. After a manuscript is technically edited and formatted, it will be removed from the "Just Accepted" Web site and published as an ASAP article. Note that technical editing may introduce minor changes to the manuscript text and/or graphics which could affect content, and all legal disclaimers and ethical guidelines that apply to the journal pertain. ACS cannot be held responsible for errors or consequences arising from the use of information contained in these "Just Accepted" manuscripts.

ACS Publications

ACS Applied Materials & Interfaces is published by the American Chemical Society.
1155 Sixteenth Street N.W., Washington, DC 20036

Published by American Chemical Society. Copyright © American Chemical Society. However, no copyright claim is made to original U.S. Government works, or works produced by employees of any Commonwealth realm Crown government in the course of their duties.

Supercapattery based on binder-free $Co_3(PO_4)_2 \cdot 8H_2O$ multilayer nano/ microflakes on nickel foam

Han Shao[a,b], N. Padmanathan[a], David McNulty[b], Colm O'Dwyer[a,b] and Kafil. M. Razeeb[a,]*

[a]Micro-Nano Systems Centre, Tyndall National Institute, University College Cork, Dyke Parade, Lee Maltings, Cork T12 R5CP, Ireland

[b]Department of Chemistry, University College Cork, Cork T12 YN60, Ireland

*Corresponding Author: Dr. Kafil M. Razeeb (kafil.mahmood@tyndall.ie)

KEYWORDS: Cobalt phosphate hydrate, Nanomaterial, Supercapattery, Supercapacitor, Electrochemical, Energy Storage Device.

Abstract

A binder-free cobalt phosphate hydrate ($Co_3(PO_4)_2 \cdot 8H_2O$) multilayer nano/ microflakes structure is synthesized on nickel foam (NF) via a facile hydrothermal process. Four different concentrations (2.5 mM, 5mM, 10mM and 20mM) of the Co^{2+} and PO_4^{-3} were used to obtain different mass loading of cobalt phosphate on the nickel foam. The $Co_3(PO_4)_2 \cdot 8H_2O$ modified NF electrode (2.5 mM) shows a maximum specific capacity of 868.3 C g^{-1} (capacitance of 1578.7 F g^{-1}) at a current density of 5 mA cm^{-2} and remains as high as 566.3 C g^{-1} (1029.5 F g^{-1}) at 50 mA cm^{-2} in 1 M NaOH. A supercapattery assembled using $Co_3(PO_4)_2 \cdot 8H_2O$/NF as positive and activated carbon/NF as negative electrode, delivers a gravimetric capacitance of 111.2 F g^{-1} (volumetric capacitance of 4.44 F cm^{-3}). Furthermore, the device offers a high specific energy of 29.29 Wh kg^{-1} (energy density of 1.17 mWh cm^{-3}) and a specific power of 4687 W kg^{-1} (power density of 187.5 mW cm^{-3}).

Introduction

Supercapattery, as the ideal electrochemical energy storage device, combines the high energy-storage capability of conventional batteries with the high power-delivery-capability of supercapacitors. A large amount of investigations have been carried out in the development of this hybrid energy storage device to combine the best of both worlds[1-4]. Till date many researchers have classified their work to be capacitive which showed battery-like behaviour due to the misunderstanding of pseudocapacitor and supercapattery.[5-8] "Pseudocapacitance" is used to describe the electrode materials with similar electrochemical properties to a capacitive carbon electrode, such as RuO_2 and MnO_2, which exhibits a rectangular cyclic voltammograms (CV) and a triangular charge-discharge curve[9-10]. The new terminology of supercapattery was created to define the electrochemical behaviour between capacitor-like and battery-like hybrids. In addition, the so-called asymmetric supercapacitors fabricated by using redox materials as positive electrode and carbon based materials as negative electrode were also miscalled, which should also be named hybrid supercapattery. [8, 11]

In recent years, several groups proposed to apply transition metal phosphates and their composites as electrode materials for supercapattery due to their good performance as positive electrode materials for rechargeable ion-batteries.[1, 12-14] However, for cobalt phosphate, only limited reports are available for supercapattery applications and none on a complete cell.

Li et al. fabricated a 3D $Co_3(PO_4)_2 \cdot 8H_2O$ architecture with a specific capacitance of 350 F g^{-1} at an applied current of 1 A g^{-1} [15] whereas, *Tang et al.* reported a honeycomb-like mesoporous $Co_3(PO_4)_2 \cdot 8H_2O$ nanospheres with a specific capacitance of 247.7 F g^{-1} at a current of 0.25 A g^{-1}.[16] Three different cobalt based composites namely, $Co_{11}(HPO_3)_8(OH)_6$, $CoHPO_3 \cdot 3H_2O$ and $NH_4CoPO_4 \cdot H_2O$ were fabricated using hydrothermal process, delivered a specific capacitance of

312, 413 and 369.4 F g^{-1}, respectively.[17-19] . All these single electrodes showed a low specific capacitance and thereby will not be able to deliver more energy density than existing carbon or oxide based electrodes[20-21]. Furthermore, *Wang et al.* reported a mesoporous uniform $NH_4NiPO_4 \cdot H_2O$ nanostructure with a specific capacitance of 1072 F g^{-1} at a current of 1.5 A g^{-1}.[22] Nevertheless, none of the above work realized a complete cell to further study the electrochemical performance of the cobalt phosphate composites.

In terms of complete cells, a capacitance of 80.5 F g^{-1} was reported for an asymmetric supercapacitor using $Mn_3(PO_4)_2 \cdot 3H_2O$ nanosheets as positive electrode and activated carbon (AC) as negative electrode.[23] *Tang et al.* reported a cobalt nickel phosphate nanospheres // AC hybrid supercapattery with a good capacitance of 149.6 F g^{-1}.[16] *Gao et al.* investigated an ultrathin hybridized phosphate ($(NH_4)(Ni, Co)PO_4 \cdot 0.67H_2O$) nanoslices // AC hybrid device exhibited a specific capacitance of 78 F g^{-1}.[23] Hierarchical 1D $NH_4NiPO_4 \cdot H_2O$ microrods achieved an aerial capacitance of 66 mF cm^{-2} in a flexible all-solid-state supercapacitor.[24] Among these complete cells, the highest specific energy of 45.8 Wh kg^{-1} was reported for $Co_{0.86}Ni_{2.14}(PO_4)_2$ // AC but the cycle stability is quite low, which is only 66.5% after 1000 cycles.[16]

Herein, we report a cobalt phosphate hydrate ($Co_3(PO_4)_2 \cdot 8H_2O$) multilayer nano/ microflakes structure synthesized on nickel foam by a hydrothermal method. The electrochemical performance of the material was tested as single electrode and as the positive electrode of a supercapattery cell in 1.0 M NaOH electrolytes. The specific capacity of this binder-free multilayer nano/ microflake structured material is 868.3 C g^{-1} (241.2 mAh g^{-1}) at a current density of 5 mA cm^{-2}, which is equivalent to a specific capacitance of 1578.7 F g^{-1}. The capacity retention is 65.2% (566.3 C g^{-1}, 157.3 mAh g^{-1}, 1029.5 F g^{-1}) of the initial value at a current

density of 50 mA cm^{-2}. The hybrid device in a configuration of $Co_3(PO_4)_2 \cdot 8H_2O$/NF // separator // AC/NF delivers a high specific capacitance of 111.2 F g^{-1} and a specific energy of 29.29 Wh kg^{-1} (energy density of 1.17 mWh cm^{-3}) at a specific power of 468.75 W kg^{-1} (power density of 18.75 mW cm^{-3}), with an excellent cyclic stability of 77.9% after 1000 cycles. Compared to the state of the art mono-metallic phosphate based electrode materials, our electrode showed increased capacity (capacitance) and energy density with excellent cyclic stability.

Experimental Section

Material Synthesis:

$Co_3(PO_4)_2 \cdot 8H_2O$ nano/ microflakes were synthesized by hydrothermal method on nickel foam (NF). In detail, nickel foam (3×3 cm^2) treated with 3 M HCl followed by washing with ethanol and deionized water for 15 minutes was used as substrate. Equal concentration (2.5 mM) of $Co(NO_3)_2 \cdot 6H_2O$ and $NH_4H_2PO_4$ were dissolved in deionized (DI) water under stirring for 15 min. The solution was transferred to a 100 ml reaction vessel, which contained the pre-treated nickel foam substrate and was then kept at 120 °C for 8 h in oven. After this time, the reaction vessel was allowed to cool down to room temperature naturally. Finally, substrates covered with $Co_3(PO_4)_2 \cdot 8H_2O$ were washed with DI water several times with the assistance of ultrasonication, and then dried in air. For the mass loading study, different concentrations (5 mM, 10 mM, 20 mM) of Co^{+2} and PO_4^{-3} were prepared using the same procedure. The amount of $Co_3(PO_4)_2 \cdot 8H_2O$ was measured from the weight difference of the pure nickel foam and $Co_3(PO_4)_2 \cdot 8H_2O$ grown nickel foam. Typical mass of the active electrode material is ~4, ~8, ~11 and ~15 mg/cm^2, respectively. Figure S1 in the Electronic Supplementary Information (ESI) shows a photograph of $Co_3(PO_4)_2 \cdot 8H_2O$/NF samples prepared using different concentrations (2.5 mM, 5 mM, 10 mM, 20 mM).

Materials Characterization:

The crystal structures of $Co_3(PO_4)_2 \cdot 8H_2O$/NF samples were analysed using X-ray diffractometer (XRD Philips PW3710-MPD diffractometer with Cu Kα radiation, λ=1.54Å). The surface morphology and compositional analysis of $Co_3(PO_4)_2 \cdot 8H_2O$/NF samples were performed

by field emission scanning electron microscope (FEI QUANTA 650 HRSEM) with an energy dispersive X-ray spectroscopy (EDX Oxford Instruments INCA energy system) and high resolution transmission electron microscope (JEOL HRTEM-2100 at 200 kV). To avoid contribution of Ni from the NF, the EDX and TEM measurements were carried out for the powder samples scratched off from the NF. The Raman spectra of $Co_3(PO_4)_2 \cdot 8H_2O$/NF hybrid structures were recorded with the Renishaw (RA 100) inVia confocal Raman Microscope at 514.5 nm excitation. The X-ray photoelectron spectroscopy (XPS) analysis was performed on a Kratos Ultra DLD spectrometer with Al K α (1486.6 eV) as the X-ray source.

Electrochemical Measurement:

The electrochemical performance of the $Co_3(PO_4)_2 \cdot 8H_2O$/NF electrodes were investigated in a three-electrode system at 25 ºC. The nickel foam supported $Co_3(PO_4)_2 \cdot 8H_2O$, platinum wire and saturated calomel electrode (SCE) were used as working, counter and reference electrodes, respectively. The electrolyte was 1.0 M NaOH solution. The electrochemical properties of hybrid cell were evaluated in a two-electrode system using $Co_3(PO_4)_2 \cdot 8H_2O$/NF as positive electrode and activated carbon/NF as negative electrode separated by Celgard separator in 1.0 M sodium hydroxide solution. The activated carbon (AC) based electrode was prepared by mixing 90 wt% AC and 10 wt% PVDF (polyvinylidene difluoride) and spreading the mixture on to a 3 × 3 cm^2 nickel foam. Typical mass loading of 2, 4 and 6 mg cm^{-2} were used to fabricate activated carbon electrode. Both positive and negative electrodes were cut into 1 × 1 cm^2 then assembled into a hybrid supercapattery. The electrochemical measurements, including cyclic voltammetry (CV), chronopotentiometry, and A. C. impedance techniques were conducted using a CHI 660C electrochemical workstation and a Bio-logic VSP Modular 5 channels potentiostat.

Results and Discussion

X-ray diffraction (XRD) and Raman spectroscopy were used to explore the phase structure of $Co_3(PO_4)_2 \cdot 8H_2O$ nano/ microflakes. As shown in Figure 1(a), except the marked peaks of nickel foam (peaks at 44.6°, 51.9° and 76.6°) single phase of $Co_3(PO_4)_2 \cdot 8H_2O$ were formed. All the other peaks can be indexed to the planes of cobalt phosphate hydrate (JCPDS NO. 41-0375). With increasing concentration, the peak intensity of $Co_3(PO_4)_2 \cdot 8H_2O$ increased (Figure S2), while the peak intensity of nickel decreased due to larger mass loading for higher concentration samples. Figure 1(b) shows the Raman spectra of nickel foam and $Co_3(PO_4)_2 \cdot 8H_2O$/NF. No obvious peaks were obtained from acid pre-treated pure nickel foam spectroscopy, because of no changes in polarization in the pure metal. In the spectroscopy of $Co_3(PO_4)_2 \cdot 8H_2O$/NF, the peaks due to the Ni-O stretching at 560 cm^{-1} indicated the conversion of the nickel foam which is presented in Section 5 of the ESI.[25] O-Co-O bending appears at 260 and 370 cm^{-1}.[26] The O-P-O bending modes are located at 462 cm^{-1},[27-28] while the symmetric O-P-O stretching vibrations are observed at 956, 1023 and 1046 cm^{-1}. [26 27-28] The asymmetric P-O-P stretching vibration was obtained at 894 cm^{-1}.[28] The external modes are found in the 160-250 region.[28-29] All these modes confirm the formation of $Co_3(PO_4)_2 \cdot 8H_2O$ composite on nickel foam[26, 28, 30-31].

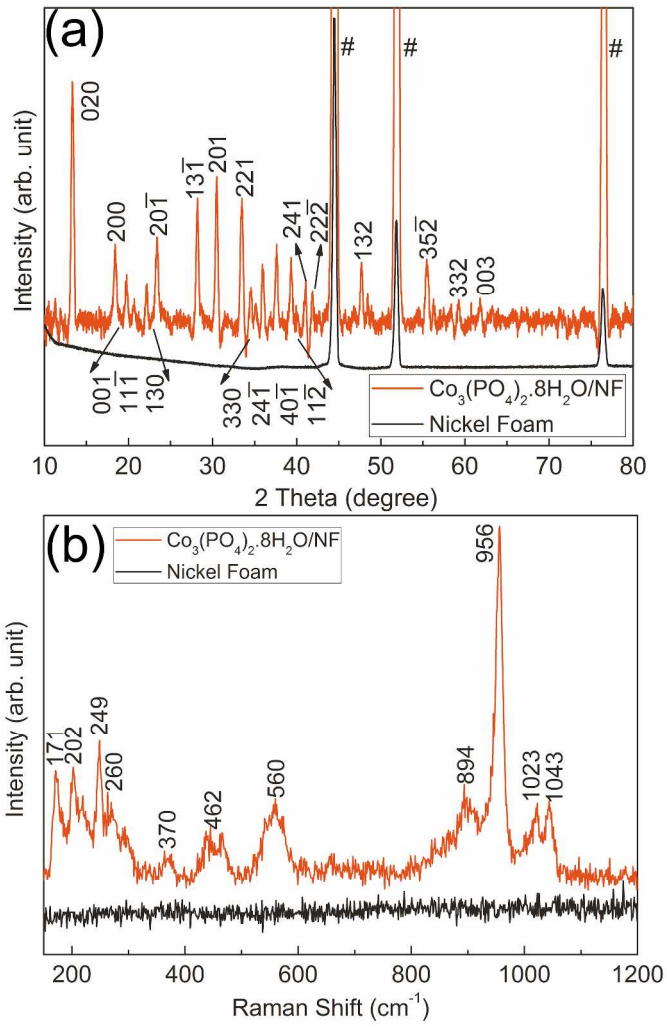


Figure 1. (a) XRD pattern and (b) Raman spectra of pure nickel foam and 2.5 mM $Co_3(PO_4)_2 \cdot 8H_2O$/NF nano/microstructure.

Figure 2 shows the SEM images of nickel foam supported $Co_3(PO_4)_2 \cdot 8H_2O$ nano/ microflakes at different magnifications fabricated from 2.5 mM concentration. Low magnification images (Figure 2a, b) shows the homogeneous growth of the $Co_3(PO_4)_2 \cdot 8H_2O$ multilayer nano/ microflakes. These nano/ microflakes were formed layer by layer with an average thickness ranging from 400 nm to 1 μm as can be seen in Figure 2(c, d). With increasing concentration (from 2.5 to 20 mM), individual layer of the multilayer structures grew thicker (600 nm to 1.2

μm) in a disorderly fashion into different directions as can be observed in Figure S3-S4. Thicker flakes easily block the interspace of the nickel foam and might reduce the overall surface area of the electrode. To analyze the component in the nano/ microflakes structure, thin flake-powder was scratched off from the nickel foam and stuck to the copper tape. The elemental mapping on the flakes in Figure 2(e) clearly shows the distribution of Co, P and O, which is in good agreement with the XRD and Raman analysis.

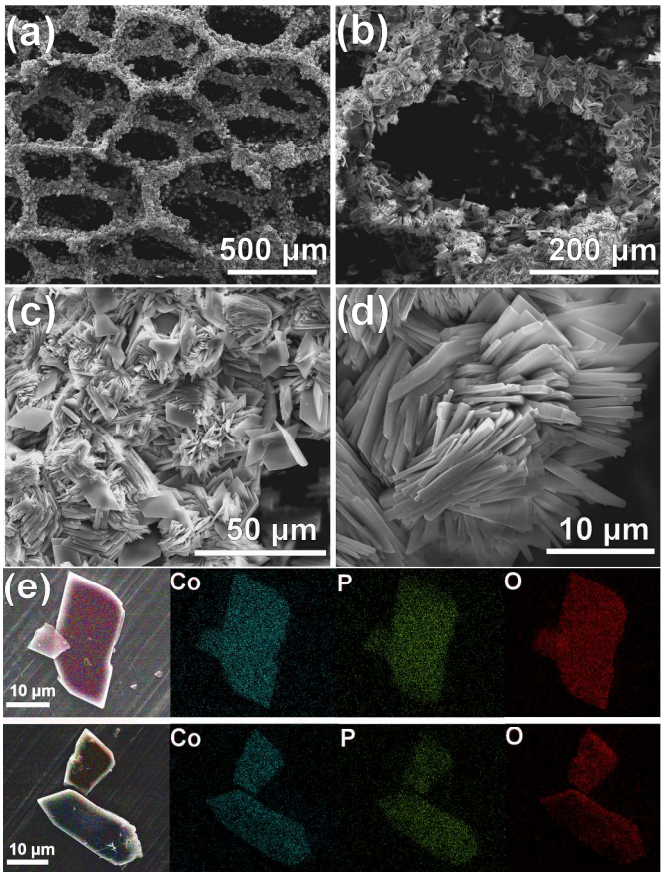


Figure 2. (a-d) SEM images of 2.5 mM $Co_3(PO_4)_2 \cdot 8H_2O$/NF nano/microflakes at different magnifications (e) Elemental mapping spectrum of $Co_3(PO_4)_2 \cdot 8H_2O$/NF nano/microstructure scanned at different flake-powder.

In addition, high-resolution transmission electron microscopy (HR-TEM) measurements were carried out for the powder samples scratched off from the nickel foam to avoid the contribution of the substrate. The HR-TEM and corresponding selected-area electron diffraction (SAED) images are shown in Figure 3. Different thicknesses of scratched powder sample were selectively analyzed. Figure 3(a) and (b) clearly show a single layer found at the edge of a thick sample piece, which is comprised of several layers. Similarly, Figure 3(c) demonstrates the obvious layer-by-layer structure, confirming the multilayer structure shown in the SEM images in Figure 2(c-d). The corresponding SAED pattern in Figure 3(d) shows the electron diffraction from different planes and is consistent with XRD results.

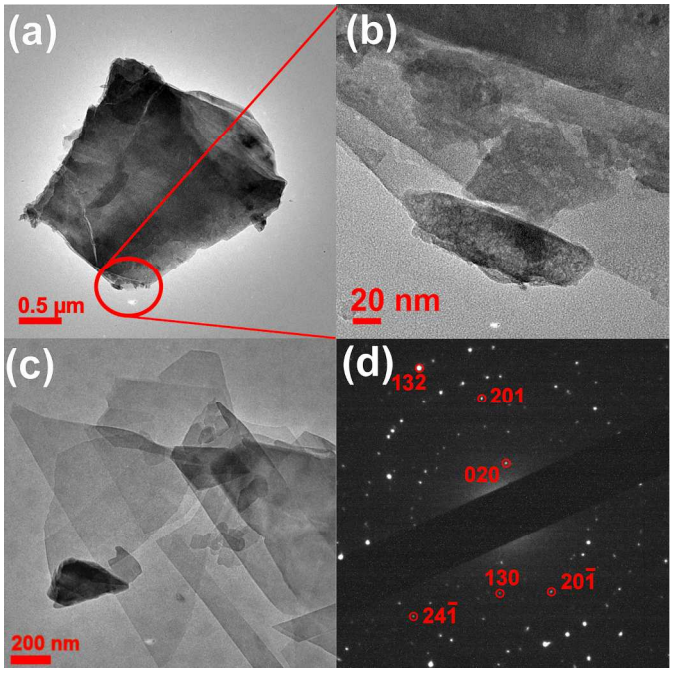


Figure 3. (a-c) HRTEM images of $Co_3(PO_4)_2 \cdot 8H_2O$ multilayer structure, (d) corresponding SAED pattern.

The samples were further analyzed by XPS to investigate the appropriate valence states. Figure S6 in ESI represents the XPS spectra of pure nickel foam and $Co_3(PO_4)_2 \cdot 8H_2O$/NF samples. A

brief description of the XPS data and analysis is presented in Section 2 of the ESI, which is in good agreement with the XRD and Raman analysis.

To investigate the electrochemical performance of the $Co_3(PO_4)_2 \cdot 8H_2O$/NF, a three electrode system was used. Figure S7(a) shows the CV curves of pure nickel foam, 2.5, 5, 10 and 20 mM $Co_3(PO_4)_2 \cdot 8H_2O$/NF at a scan rate of 2 mV/s in 1.0 M NaOH solution. The contribution of bare nickel foam is negligible compare to the $Co_3(PO_4)_2 \cdot 8H_2O$. Clear current peaks are observed in all the samples, indicating the non-capacitive faradaic energy storage properties of the electrode material. With increasing concentration (i.e., with increased mass loading of the active material), the main peaks around 0.45 and 0.25 V broaden and the peak current varies. This may be due to the higher mass loading, which results in more activate material to take part in the redox reaction but on the other hand reduces the conductivity of the electrode as can be observed from the Nyquist plots in Figure S8. The resistance of the electrodes are found to be 1.90, 1.94, 2.47 and 4.8 Ω with increased mass loading. The 2.5 and 5 mM CVs are nearly symmetrical, indicating good redox property of the material. However, for higher concentration samples, the secondary peaks (around 0.25 and 0.55 V) become more obvious because of the larger mass loading enhanced the first step of the redox reactions (shown as equation 1). Two pairs of oxidation and reduction peaks indicate the transform between the different states of Co^{2+} and Co^{3+}. Figure 4(a) shows the CV curves of 2.5 mM sample at different scan rate from 1 to 50 mV/s. With increasing scan rate, the oxidation and reduction peaks started to shift from each other, indicating quasi-reversible reaction and the shape of the CVs tends to be asymmetric. Figure S7(b) shows that the peak shift in 5 mM sample is less than 2.5 mM sample, which may be due to the larger loading (2× compared to 2.5 mM) of cobalt phosphate, resulted in more active materials to be involved in the faradaic reactions as follows[32-33]:

$$Co_3(PO_4)_2.8H_2O + OH^- \leftrightarrow Co_3(PO_4)_2(OH^*) + e^- \quad (1)$$

$$Co_3(PO_4)_2(OH^*) + OH^- \leftrightarrow Co_3(PO_4)_2(O^*) + H_2O + e^- \quad (2)$$

$$O^* + O^* \leftrightarrow O_2\uparrow \quad (3)$$

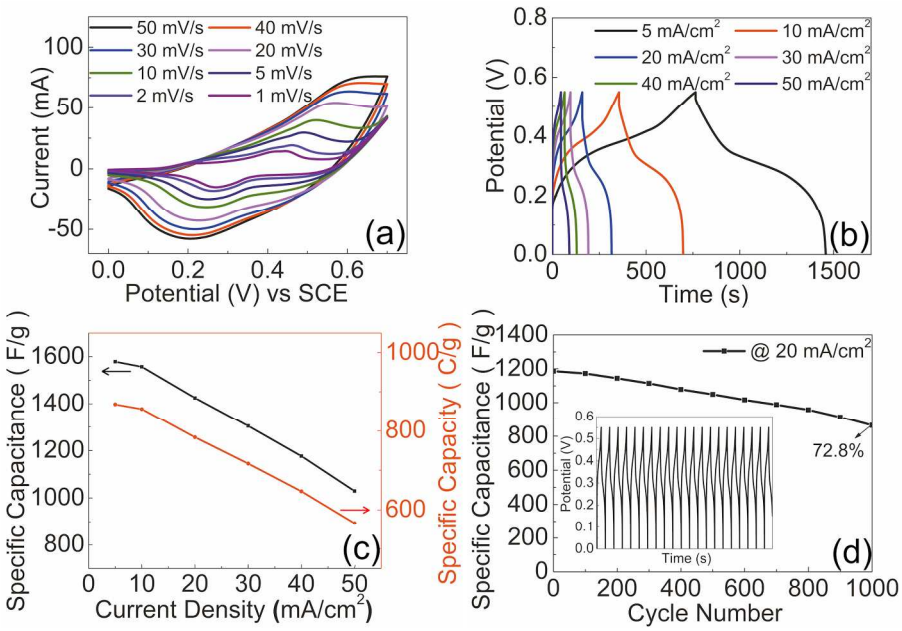


Figure 4. (a) Cyclic voltammograms of 2.5 mM $Co_3(PO_4)_2 \cdot 8H_2O$/NF at different scan rate from 1 to 50 mV/s in 1 M NaOH. (b) Charge-discharge profile of the electrode at different current densities. (c) Specific capacitance and capacity variation at different current densities. (d) Cyclic stability of the electrode. Inset represents continuous charge-discharge profile at 20 mA/cm^2.

Figure 4(b) shows the charge-discharge profile of 2.5 mM $Co_3(PO_4)_2 \cdot 8H_2O$/NF. In both 2.5 and 5 mM discharging curves (Figure S7(c) and (d)), distinct potential plateaus are observed, which demonstrate the battery-like characteristics of the electrodes. The nearly symmetric charging and discharging curves at low current density indicate the reversible redox reaction. 5 mM sample shows nearly twice discharging time than the 2.5 mM sample at similar current density, which may be due to double mass loading in case of 5 mM sample. However, for 10 and

20 mM samples (Figure S7(e-f)), the discharge time does not increase with larger mass loading. From SEM image analysis in Figure S4 we found that the multilayer structures for higher-concentration samples grew thicker and larger in a disorderly fashion, which reduces the overall surface area of the electrode accessible by the electrolyte and thereby less active material is taking part in storing the charge. These results are in good agreement with the CV analysis presented in Figure 4(a) and Figure S7(a).

Due to the non-capacitive faradaic (or battery) mechanism, the specific capacity in terms of C g^{-1} or mAh g^{-1} was calculated using equations 1 and 2 as described in section 3 of ESI. A maximum specific capacity of 868.3 C g^{-1} (241.2 mAh g^{-1}) at an applied current density of 5 mA cm^{-2} was found for the 2.5 mM sample. The capacity variation as a function of current density is shown in Figure 4(c). With a 10 times increase in the current density (from 5 to 50 mA cm^{-2}), the capacity retention is 65.2% and 72.1% of the initial value for 2.5 and 5 mM samples, which are much better than the state of the art (48%) cobalt phosphate electrodes.[15]

However, to be comparable with reported literatures, specific capacitance in terms of F g^{-1} was calculated using equation 3 as shown in section 3 of ESI. An ultra-high specific capacitance of 1578.7 F g^{-1} was achieved from 2.5 mM $Co_3(PO_4)_2 \cdot 8H_2O$/NF at 5 mA cm^{-2} (1.25 A/g) and 1336.9 F g^{-1} was attained for 5 mM sample at 5 mA cm^{-2} (0.625 A/g), and reduced to 1029.5 F g^{-1} (65.2%) for 2.5 mM and 963.6 F g^{-1} (72.1%) for 5 mM sample for a current density of 50 mA/cm^2 (Figure 4(c) and Figure S9). The reduction in specific capacitance in the 5 mM and higher concentration samples are due to the larger mass loading, which resulted in a thicker layer formation as compared to low concentration sample that ultimately reduced the active sites for ion diffusion from the electrolyte. However, the specific capacitance for 2.5 mM electrode is found to be better than the work reported by Tang et al., where a specific capacitance of 1409.8 F

g^{-1} at 0.25 A g^{-1} was obtained for a honeycomb-like mesoporous cobalt nickel phosphate nanospheres, whereas for $Co_3(PO_4)_2$, only 247.7 F g^{-1} was reported[16]. Similarly, *Li et al.* showed 350 F g^{-1} at 1 A g^{-1} for a 3D $Co_3(PO_4)_2 \cdot 8H_2O$ architecture with flower-like morphologies assembled from 2D microsheets.[15] Furthermore, *Pang et al.* reported three different phosphate microstructures, and achieved 312 F g^{-1} for $Co_{11}(HPO_3)_8(OH)_6$ nanoribbons [17], 413 F g^{-1} for $CoHPO_4 \cdot 3H_2O$ nanosheets and 369.4 F g^{-1} for $NH_4CoPO_4 \cdot H_2O$ nano/microstructures. Whereas, our 2.5 mM electrode showed ~4 times better specific capacitance as compared to the best reported cobalt phosphate based electrodes. Table S1 and Table S3 compares the specific capacity and capacitance of all the four different concentration electrodes fabricated in this work and other similar metal phosphate and cobalt oxide based electrode materials and from published literature.[15-19, 22-24, 34] Another important requirement for supercapattery application is the long term cyclic stability. Figure 4(d) shows the cyclic stability of the 2.5 mM sample and the inset shows the continuous charge-discharge profile at 20 mA/cm^2. The electrode exhibited a capacitance of 1149 F g^{-1} (72.8% retention) after 1000 cycles, which is more than twice of the best capacitance value reported for cobalt phosphate based electrodes.[15-18] The decrease of the capacitance after 1000 charge-discharge cycles may be due to the morphology transformation and the dissolution of the active material as shown in Figure S16.

It is noteworthy that the observed specific capacity (or capacitance) is higher than the theoretical value (533 C g^{-1} or 969 F g^{-1} as calculated by Equation 8 and 9 as shown in section 3 of ESI [35]) for the cobalt phosphate electrode. This may be attributed to the contribution of electric double layer capacitance in addition to the battery-like faradaic contributions.[36] When crystalline water is removed from the $Co_3(PO_4)_2 \cdot 8H_2O$ during electrochemical reaction, a large amount of void space is available for redox reaction. The interconnected $Co_3(PO_4)_2$ nanosheets

are favorable for electrolyte penetration to the interior surfaces via the intercalated water molecules. After oxidation of crystalline water, there is a possibility of forming abundant pores within the $Co_3(PO_4)_2$ nano/ microsheets as can be seen in Figure S5 of ESI, which provide large surface area and numerous electroactive sites for effective ion adsorption.

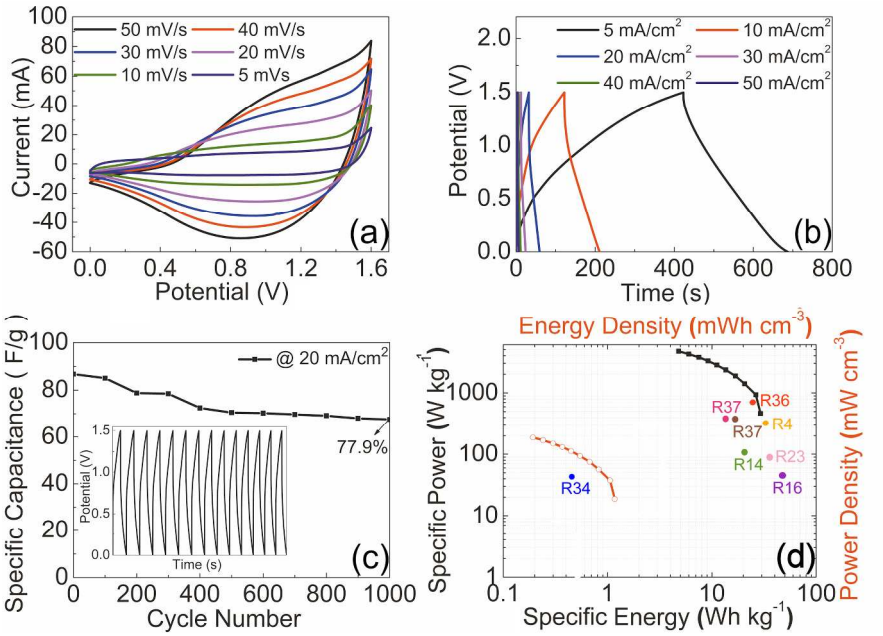


Figure 5. (a) Cyclic voltammograms of the $Co_3(PO_4)_2 \cdot 8H_2O$//AC hybrid supercapattery at different scan rates in 1 M NaOH. (b) Charge-discharge curves of supercapattery at different current densities. (c) Cyclic stability of supercapattery. Inset represents continuous charge-discharge profile at 20 mA/cm^2 (d) Ragone plots of supercapattery.[4, 14, 16, 23, 34, 36-37]

In order to evaluate the performance of our $Co_3(PO_4)_2 \cdot 8H_2O$/NF electrode, a hybrid supercapattery ($Co_3(PO_4)_2 \cdot 8H_2O$//AC) was assembled with 2.5 mM $Co_3(PO_4)_2 \cdot 8H_2O$/NF as positive electrode and AC/NF as negative electrode in 1 M NaOH solution. A brief discussion on the optimization of the positive and negative electrodes for the hybrid supercapattery is presented

in Section 4 of the ESI. Typical mass loading of 2, 4 and 6 mg cm^{-2} were used to fabricate the activated carbon electrode. Among those, 4 mg cm^{-2} mass loading of activated carbon showed the best performance due to the balance of the charge flow between the positive electrode and the negative electrode. Figure 5(a) shows the CV curves of the $Co_3(PO_4)_2 \cdot 8H_2O$//AC supercapattery at different scan rates from 5 to 50 mV/s. The quasi-rectangle shapes of these CV curves demonstrate the dominant capacitive behaviour rather than battery characteristic. The CV curves retain the same shape with increasing scan rate, which exhibited a good rate capability of the hybrid supercapattery. The individual CV curves of positive ($Co_3(PO_4)_2 \cdot 8H_2O$/NF) and negative (AC/NF) electrodes are shown in Figure S10 (c). The negative electrode demonstrated a typical electric double layer charge-discharge profile, with hydrogen storage at deep cathodic conditions. On the other hand, the positive electrode has a capacity of redox reversible reaction. Thereby, a potential window of 1.6 V was achieved in this hybrid supercapattery. Figure 5(b) shows the charge-discharge curves of the $Co_3(PO_4)_2 \cdot 8H_2O$//AC supercapattery at different current densities with a cell voltage up to 1.5 V. Quasi-lined charge and discharge curves rather than potential plateaus confirm the capacitive characteristic of the hybrid supercapattery. Specific capacitances at different current densities (Figure S11) were calculated by equation 4 and 5 (ESI), based on the total mass of both positive and negative active materials (~8 mg) or the total measured volume of the hybrid supercapattery (0.2 cm^{-3}).

The device showed a specific capacitance of 111.2 F g^1 (4.44 F cm^{-3}) at a current density of 5 mA cm^{-2}. Even at 50 mA cm^{-2}, it showed a specific capacitance of 50.7 F g^1 (2.03 F cm^{-3}). Thereby, our hybrid device could retain a remarkable 45.6% of the initial value for ten times of initial current density. Furthermore, the hybrid supercapattery showed better cyclic stability of 77.9% (Figure 5(c)) after 1000 cycles as compared to the earlier reported work (66.5% and

57.8%)[16]. Compared to three electrode system, the hybrid supercapattery exhibits a better cyclic stability, which may be due to the synergistic effect of the positive supercapattery electrode with the negative carbon based electrode, which reduced the dissolution of active material.

Due to the non-linear function of the charge-discharge curves, the specific energy (density) and specific power (density) were calculated by equations 6 and 7 as shown in the ESI. As in the Ragone plots shown in Figure 5(d) and Table S2, the highest specific energy was found to be 29.29 Wh kg^{-1} (energy density of 1.17 mWh cm^{-3}) at a specific power of 468.75 W kg^{-1} (power density of 18.75 mW cm^{-3}) for the hybrid device using 2.5 mM $Co_3(PO_4)_2 \cdot 8H_2O$/NF as positive and AC/NF as negative electrode. Even at a high specific power of 4687 W kg^{-1} (power density of 187.5 mW cm^{-3}), the device could retain a specific energy of 5.33 Wh kg^{-1} (energy density of 0.21 mWh cm^{-3}). The Nyquist plot of the hybrid supercapattery before and after 1000 cycles is shown in Figure S12. From the two plots, resistance was found to be only 0.80 Ω and 5.06 Ω for the hybrid supercapattery before and after cyclability test, which indicate acceptable conductivity for the device even after 1000 cycles.

Overall, cobalt phosphate hydrate multilayer nano/ microflakes structure showed interesting properties as a positive electrode for supercapattery application. Lower concentration samples exhibited better electrochemical performance due to the less mass loading and thinner layer and showed state of the art specific capacitance for this composite. Formation of $Co_3(PO_4)_2 \cdot 8H_2O$ nano/ microflakes coupled with mesoporous Ni foam resulted in a large contact area between active materials and the electrolyte, leading to more efficient ion and charge transport, resulting in significant increases in the specific capacitance and rate capability at high current densities. Thereby, the hybrid device showed excellent specific capacitance with very good energy and power density, acceptable retention capability and good cyclability.

Conclusions

In summary, we reported a binder-free $Co_3(PO_4)_2 \cdot 8H_2O$ multilayer nano/ microflakes structure via simple hydrothermal technique on nickel foam substrate as a positive electrode for supercapattery application. Due to the different concentrations of the synthesis process, different mass loading of the active materials were achieved. Single phase of $Co_3(PO_4)_2 \cdot 8H_2O$ were formed homogeneously over the nickel foam with an average thickness of 400 nm to 1 μm. Among all the samples, the highest specific capacity of 868.3 C g^{-1} (241.2 mAh g^{-1}) at a current density of 5 mA cm^{-2} was exhibited from 2.5 mM sample, with a rate capability of 65.2% for 10 times of the initial current density. A high performance hybrid supercapattery was fabricated using $Co_3(PO_4)_2 \cdot 8H_2O$/NF as positive and AC/NF as the negative electrode. A maximum specific energy of 29.29 Wh kg^{-1} (energy density of 1.17 mWh cm^{-3}) was obtained at a specific power of 468.75 W kg^{-1} (power density of 18.75 mW cm^{-3}), with good cyclic stability of 77.9% after 1000 cycles. Therefore, $Co_3(PO_4)_2 \cdot 8H_2O$ can be a promising material for supercapattery application.

ASSOCIATED CONTENT

Supporting Information

The supporting information is available free of charge on the ACS publications website at DOI:

Mass loading study, XRD pattern, SEM images, CV graphs, discharge curves, Nyquist plot, specific capacitance, of 2.5 mM, 5 mM, 10 mM and 20 mM $Co_3(PO_4)_2 \cdot 8H_2O$/NF nano/microflakes; HRTEM image of $Co_3(PO_4)_2 \cdot 8H_2O$ with particle analysis; XPS spectra of pure nickel foam and $Co_3(PO_4)_2 \cdot 8H_2O$/NF; specific capacitance, capacity, energy density, power density calculations; tables of comparison of our work, other phosphate based electrodes, other cobalt oxide based electrodes and other phosphate based electrodes devices; optimization of positive and negative electrodes for hybrid supercapattery; specific capacitance as a function of applied current for hybrid supercapattery; Nyquist plot for $Co_3(PO_4)_2 \cdot 8H_2O$//AC hybrid supercapattery before and after 1000 cycles; growth mechanism of $Co_3(PO_4)_2 \cdot 8H_2O$ multilayer nano/ microflakes on nickel foam; SEM images of $Co_3(PO_4)_2 \cdot 8H_2O$/NF electrode after 1000 charge-discharge cycles.

AUTHOR INFORMATION

Corresponding Author

Dr. Kafil M. Razeeb, Nano-Interconnection, Tyndall National Institute, University College Cork, Dyke Parade, Lee Maltings, Cork T12 R5CP, Ireland. Phone: +353 21 2346078, E-mail: kafil.mahmood@tyndall.ie.

Author Contributions

The manuscript was written through contributions of all authors. All authors have given approval to the final version of the manuscript.

Notes

The authors declare no competing financial interest.

Funding Sources

EU FP7 project MANpower (contract number: 604360)

ACKNOWLEDGMENT

The authors acknowledges the financial support from EU FP7 project MANpower (contract number: 604360) to carry out this work. We acknowledge support from Science Foundation Ireland under a Technology Innovation and Development Award no. 14/TIDA/2455.

ABBREVIATIONS

NF, nickel foam; XRD, X-ray diffractometer; SEM, scanning electron microscope; EDX, energy dispersive X-ray spectroscopy; TEM, transmission electron microscope; XPS, X-ray photoelectron spectroscopy; CV, cyclic voltammograms; AC, activated carbon; ESI, electronic supplementary information;

REFERENCES

1. Sundaram, M. M.; Watcharatharapong, T.; Chakraborty, S.; Ahuja, R.; Duraisamy, S.; Rao, P. T.; Munichandraiah, N., Synthesis, and Crystal and Electronic Structure of Sodium Metal Phosphate for Use as a Hybrid Capacitor in Non-aqueous Electrolyte. *Dalton trans.* **2015,** *44* (46), 20108-20120.

2. Dubal, D. P.; Ayyad, O.; Ruiz, V.; Gomez-Romero, P., Hybrid Energy Storage: the Merging of Battery and Supercapacitor Chemistries. *Chem. Soc. rev.* **2015,** *44* (7), 1777-1790.

3. Secchiaroli, M.; Giuli, G.; Fuchs, B.; Marassi, R.; Wohlfahrt-Mehrens, M.; Dsoke, S., High Rate Capability $Li_3V_{2-x}Ni_x(PO_4)_3$/C (x = 0, 0.05, and 0.1) Cathodes for Li-ion Asymmetric Supercapacitors. *J. Mater. Chem. A* **2015,** *3* (22), 11807-11816.

4. Dai, Y.-H.; Kong, L.-B.; Yan, K.; Shi, M.; Luo, Y.-C.; Kang, L., Facile Fabrication of Manganese Phosphate Nanosheets for Supercapacitor Applications. *Ionics* **2016,** *22*(8), 1461-1469.

5. Akinwolemiwa, B.; Peng, C.; Chen, G. Z., Redox Electrolytes in Supercapacitors. *J. Electrochem. Soc.* **2015,** *162* (5), A5054-A5059.

6. Brousse, T.; Belanger, D.; Long, J. W., To Be or Not To Be Pseudocapacitive? *J. Electrochem. Soc* **2015,** *162* (5), A5185-A5189.

7. Chen, G. Z. In Perception of Supercapacitor and Supercapattery, Meeting Abstracts, Boston, United States, The Electrochemical Society: Boston, United States, **2011**; pp 559-559.

8. Chen, G. Z., Understanding Supercapacitors Based on Nano-hybrid Materials with Interfacial Conjugation. *Prog. Nat. Sci.: Mater. Int.* **2013,** *23* (3), 245-255.

9. Subramanian, V., Mesoporous Anhydrous RuO_2 as a Supercapacitor Electrode Material. *Solid State Ionics* **2004,** *175* (1-4), 511-515.

10. Wei, W.; Cui, X.; Chen, W.; Ivey, D. G., Manganese Oxide-based Materials as Electrochemical Supercapacitor Electrodes. *Chem. Soc. rev.* **2011,** *40* (3), 1697-1721.

11. Di Hu; Chuang Peng; Chen, G. Z., Electrodeposition of Nonconducting Polymers: Roles of Carbon Nanotubes in the Process and Products. *ACS Nano* **2010,** *4* (7), 4274-4282.

12. Sun, Y.; Gai, L.; Zhou, Y.; Zuo, X.; Zhou, J.; Jiang, H., Polyhierarchically Structured TiP_2O_7/C Microparticles with Enhanced Electrochemical Performance for Lithium-ion Batteries. *CrystEngComm* **2014,** *16* (46), 10681-10691.

13. Xie, Y.; Song, F.; Xia, C.; Du, H., Preparation of Carbon-coated Lithium Iron Phosphate/titanium Nitride for a Lithium-ion Supercapacitor. *New J. Chem.* **2015,** *39* (1), 604-613.

14. Senthilkumar, B.; Sankar, K. V.; Vasylechko, L.; Lee, Y.-S.; Selvan, R. K., Synthesis and Electrochemical Performances of Maricite-$NaMPO_4$(M = Ni, Co, Mn) Electrodes for Hybrid Supercapacitors. *RSC Adv.* **2014,** *4* (95), 53192-53200.

15. Li, H.; Yu, H.; Zhai, J.; Sun, L.; Yang, H.; Xie, S., Self-assembled 3D Cobalt Phosphate Octahydrate Architecture for Supercapacitor Electrodes. *Mater. Lett.* **2015,** *152*, 25-28.

16. Tang, Y.; Liu, Z.; Guo, W.; Chen, T.; Qiao, Y.; Mu, S.; Zhao, Y.; Gao, F., Honeycomb-Like Mesoporous Cobalt Nickel Phosphate Nanospheres as Novel Materials for High Performance Supercapacitor. *Electrochim. Acta* **2016,** *190*, 118-125.

17. Pang, H.; Liu, Y.; Li, J.; Ma, Y.; Li, G.; Ai, Y.; Chen, J.; Zhang, J.; Zheng, H., Cobalt Phosphite Microarchitectures Assembled by Ultralong Nanoribbons and Their Application as Effective Electrochemical Capacitor Electrode Materials. *Nanoscale* **2013,** *5* (2), 503-507.

18. Pang, H.; Wang, S.; Shao, W.; Zhao, S.; Yan, B.; Li, X.; Li, S.; Chen, J.; Du, W., Few-Layered $CoHPO_4 \cdot 3H_2O$ Ultrathin Nanosheets for High Performance of Electrode Materials for Supercapacitors. *Nanoscale* **2013,** *5* (13), 5752-5757.

19. Pang, H.; Yan, Z.; Wang, W.; Chen, J.; Zhang, J.; Zheng, H., Facile Fabrication of $NH_4CoPO_4{\cdot}H_2O$ Nano/microstructures and Their Primarily Application as Electrochemical Supercapacitor. *Nanoscale* **2012,** *4* (19), 5946-5953.

20. Chen, T.; Dai, L., Carbon Nanomaterials for High-performance Supercapacitors. *Mater. Today* **2013,** *16* (7-8), 272-280.

21. Padmanathan, N.; Shao, H.; McNulty, D.; O'Dwyer, C.; Razeeb, K. M., Hierarchical $NiO–In_2O_3$ Microflower (3D)/ Nanorod (1D) Hetero-architecture as a Supercapattery Electrode with Excellent Cyclic Stability. *J. Mater. Chem. A* **2016,** *4* (13), 4820-4830.

22. Zhao, J.; Pang, H.; Deng, J.; Ma, Y.; Yan, B.; Li, X.; Li, S.; Chen, J.; Wang, W., Mesoporous Uniform Ammonium Nickel Phosphate Hydrate Nanostructures as High Performance Electrode Materials for Supercapacitors. *CrystEngComm* **2013,** *15* (30), 5950-5955.

23. Zhao, Y.; Chen, Z.; Xiong, D. B.; Qiao, Y.; Tang, Y.; Gao, F., Hybridized Phosphate with Ultrathin Nanoslices and Single Crystal Microplatelets for High Performance Supercapacitors. *Sci. Rep.* **2016,** *6*, 17613-17622.

24. Raju, K.; Ozoemena, K. I., Hierarchical One-Dimensional Ammonium Nickel Phosphate Microrods for High-Performance Pseudocapacitors. *Sci. Rep.* **2015,** *5*, 17629-17642.

25. Kostecki, R.; McLarnon, F., Electrochemical and In Situ Raman Spectroscopic Characterization of Nickel Hydroxide Electrodes I. Pure Nickel Hydroxide. *J. Electrochem. Soc.* **1997,** *144* (2), 485-493.

26. Ranko P. Bontchev; Milko N. Iliev; Luiz M. Dezaneti; Jacobson, A. J., Two New Open Framework Cobalt Phosphates: $NaCo_3(OH)(PO_4)_2 \cdot 1/4H_2O$ and $Na(NH_4)Co_2(PO_4) \cdot H_2O$. *Solid State Sci.* **2001,** *3*, 133-142.

27. Chapman, A.; Thirlwell, L., Spectra of Phosphorus Compounds—I the Infra-red Spectra of Orthophosphates. *Spectrochim. Acta* **1964,** *20* (6), 937-947.

28. Baril, M.; Assaaoudi, H.; Butler, I. S., Pressure-tuning Raman Microspectroscopic Study of Cobalt(II), Manganese(II), Zinc(II) and Magnesium(II) Pyrophosphate Dihydrates. *J. Mol. Struct.* **2005,** *751* (1-3), 168-171.

29. Tuschel, D., Raman Spectroscopy and Imaging of Low Energy Phonons. *Spectroscopy* **2015,** *30* (9), 18-31.

30. Preston, C. M.; Adams, W. A., A Laser Raman Spectroscopic Study of Aqueous Orthophosphate Salts. *J. Phys. Chem.* **1979,** *83* (7), 814-821.

31. Tomimatsu, Y; Kint, S; Scherer, J. R., Resonance Raman Spectra of Iron(III)-, Copper(II)-, Cobalt(III)-, and Manganese(III)-Transferrins and of Bis(2,4,6-trichlorophenolato)diimidazolecopper(II) Monohydrate, a Possible Model for Copper(II) Binding to Transferrins. *Biochemistry* **1976,** *15* (22), 4918-4924.

32. Bajdich, M.; García-Mota, M.; Vojvodic, A.; Nørskov, J. K.; Bell, A. T., Theoretical Investigation of the Activity of Cobalt Oxides for the Electrochemical Oxidation of Water. *J. Am. Chem. Soc.* **2013,** *135* (36), 13521-13530.

33. Kim, H.; Park, J.; Park, I.; Jin, K.; Jerng, S. E.; Kim, S. H.; Nam, K. T.; Kang, K., Coordination Tuning of Cobalt Phosphates towards Efficient Water Oxidation Catalyst. *Nat. Commun.* **2015,** *6*, 9253-9263.

34. Zhao, J.; Wang, S.; Run, Z.; Zhang, G.; Du, W.; Pang, H., Hydrothermal Synthesis of Nickel Phosphate Nanorods for High-Performance Flexible Asymmetric All-Solid-State Supercapacitors. *Part. Part. Syst. Charact.* **2015,** *32* (9), 880-885.

35. Zhi, M.; Xiang, C.; Li, J.; Li, M.; Wu, N., Nanostructured Carbon–metal Oxide Composite Electrodes for Supercapacitors: a Review. *Nanoscale* **2013,** *5* (1), 72-88.

36. Wang, S.; Pang, H.; Zhao, S.; Shao, W.; Zhang, N.; Zhang, J.; Chen, J.; Li, S., $NH_4CoPO_4 \cdot H_2O$ Microbundles Consisting of One-dimensional Layered Microrods for High Performance Supercapacitors. *RSC Adv.* **2014,** *4* (1), 340-347.

37. Ma, X.-J.; Zhang, W.-B.; Kong, L.-B.; Luo, Y.-C.; Kang, L., Electrochemical Performance in Alkaline and Neutral Electrolytes of a Manganese Phosphate Material Possessing a Broad Potential Window. *RSC Adv.* **2016,** *6* (46), 40077-40085.

Table of Contents Graphic

